Physica Scripta

PAPER • **OPEN ACCESS**

Impact of CF_4 plasma etching on defect formation and material properties of Al_2O_3 thin films

To cite this article: Yu-Bin An *et al* 2025 *Phys. Scr.* **100** 065947

Physica Scripta

PAPER

Impact of CF_4 plasma etching on defect formation and material properties of Al_2O_3 thin films

Yu-Bin An[1], **Da-Won Ryu**[1], **Seung-Hyun Ma**[1], **Dong-Geon Lee**[1,2], **Mi-Jin Jin**[2], **Doo-Seung Um**[3,4] and **Chang-Il Kim**[1]

[1] School of Electrical and Electronics Engineering, Chung-Ang University, Seoul 06974, Republic of Korea
[2] Center for Multidimensional Carbon Materials (CMCM), Institute for Basic Science (IBS), Ulsan 44919, Republic of Korea
[3] Department of Electronic Engineering, Jeju National University (JNU), Jeju 63243, Republic of Korea
[4] Faculty of Applied Energy System (Electronic Engineering), Jeju National University, Jeju 63243, Republic of Korea

E-mail: dsum@jejunu.ac.kr **and** cikim@cau.ac.kr

OPEN ACCESS

RECEIVED
20 March 2025

REVISED
14 April 2025

ACCEPTED FOR PUBLICATION
29 April 2025

PUBLISHED
19 May 2025

Keywords: CF_4 plasma etching, Al_2O_3 thin films, dielectric properties, defect dynamics, optical bandgap

Supplementary material for this article is available online

Abstract

Fluorine-based plasma etching of Al_2O_3 induces changes in oxygen vacancy concentrations and aluminum bond modifications, which affect the electrical properties of the thin film, leading to increased leakage currents and the formation of charge traps that degrade the device reliability. Therefore, in this study, we systematically examined the effects of CF_4 plasma etching on the structural, optical, and electrical properties of Al_2O_3 thin films, focusing on defect dynamics during processing. X-ray photoelectron spectroscopy analysis demonstrated that Al-O to Al-F bond conversion occurred during plasma etching, resulting in modified oxygen vacancy concentrations. Chemical modifications induced changes in the optical bandgap and work function with increasing radiofrequency bias power, indicating a change in the electronic band structure. Dielectric measurements indicated reduction in dielectric constant due to Al-F bond formation. These results elucidate the relationship between plasma-induced defects, including both defect generation and atomic substitution by plasma, contributing to the development of high-quality Al_2O_3 thin films for electronic applications in the future.

1. Introduction

Plasma is an ionized gas containing electrons, ions, neutral particles, and radicals, which has become an essential element in technologies such as deposition, etching, and cleaning in semiconductor processes. In particular, plasma has become a critical component for processes demanding nanometer-level precision by optimizing the material's surface reaction with high-energy ions and active radicals [1]. Plasma etching, among them, has been established as a key technology for implementing pattern transfer in semiconductor processes. This process combines physical bombardment by ions and chemical reactions by radicals to selectively remove materials, a representative example being reactive ion etching (RIE). RIE by accelerating ions using a DC bias has become an essential technology for state-of-the-art CMOS fabrication with high-density semiconductor devices by achieving high anisotropic [2].

However, defects that occur during the plasma etching process have a significant impact on device performance, and understanding and controlling these defects is important for the innovation of semiconductor manufacturing technology [3, 4]. Plasma-induced defects can be broadly categorized into physical, charging, and radiation damage [5]. Physical damage is caused by high-energy ion bombardments, which destroy the surface crystal structure of the substrate or result in the formation of an amorphous layer. When high-energy ions penetrate the substrate surface, the defect density increases due to ion implantation and rearrangement, which can eventually cause the crystal structure to collapse or the defects to accumulate on the device surface, resulting in reduced device stability due to increased leakage current [6–8]. Charging damage, on the other hand,

occurs when charges accumulate in an insulator or dielectric owing to electrons and ions in the plasma. This phenomenon poses serious problems, especially for devices that use high-k materials. Accumulated charges can distort the electric field, which can change the threshold voltage of the device or cause localized deterioration. This damage progresses over time and while the changes in device characteristics may be minimal at first, they can significantly reduce the reliability of the device in the long term [9–11]. Finally, radiation damage caused by high-energy photons, such as ultraviolet (UV) or vacuum ultraviolet (VUV) light emitted from the plasma, breaks chemical bonds and creates charge traps at dielectric-semiconductor interfaces [12–14]. These defects lead to leakage current and device performance instability in materials such as Al_2O_3, which are prone to the formation of oxygen vacancies and aluminum-related defects [15].

Al_2O_3 is an important high-k ($\kappa \approx 9$) material in semiconductor processes, and provides a wide bandgap (8.8 eV), effectively suppressing leakage current and enhancing the electrical stability of devices. In particular, it has become the preferred gate dielectric in CMOS technology due to its excellent interface quality with silicon and its ability to suppress leakage current [16, 17]. In addition, its high thermal and chemical stabilities ensure stable operation even under extreme conditions, making it suitable for power and memory devices operating at high temperatures and voltages [18, 19]. Consequently, Al_2O_3 has emerged as a cornerstone material for next-generation semiconductor devices. Al_2O_3 may be unintentionally exposed to fluorine-based plasmas such as CF_4 or SF_6 during the etching of adjacent layers in actual device processes. This situation commonly arises in advanced semiconductor processing such as gate etching in high electron mobility transistors (e.g., $SiO_2/Al_2O_3/AlGaN/GaN$), inter metal dielectric structures with an etch stop layer, or TFT fabrication with back channel etch. Such plasma exposure can generate oxygen vacancies and aluminum bond modifications during the process. These plasma-induced defects significantly affect the electrical properties of the thin film, leading to increased leakage currents and the formation of charge traps that degrade device reliability [20]. To address these challenges, it is imperative to systematically analyze the mechanisms by which defects occur during plasma etching and investigate their impact on device performance. Such studies are essential for developing optimized plasma-etching processes that minimize defects, thereby enabling the realization of high-performance semiconductor devices.

To systematically analyze these effects, we investigated the impact of defects or doping induced by CF_4 plasma etching on the characteristics of Al_2O_3 thin films. In other words, this study focuses on the chemical and structural modifications that occur in Al_2O_3 films following plasma exposure. X-ray photoelectron spectroscopy (XPS) was used to elucidate the modulation of chemical bonding, specifically the substitution of Al-O bonds with Al-F bonds and its effect on oxygen vacancy concentrations. UV–vis spectroscopy was used to evaluate the band gap modulation associated with these chemical modifications including optical characterization. Furthermore, impedance spectroscopy was adopted to analyze the changes in the dielectric constant and electrical properties to understand the effects of plasma-induced defect passivation and atomic substitution on the dielectric constant. This comprehensive investigation aims to provide insights into the impact of plasma etching processes on thin films and changes in device characteristics.

2. Experimental details

2.1. Deposition of Al_2O_3 thin films

Al_2O_3 thin films were deposited on Si (100) substrates (P^+ and N^+ types doped with boron and arsenic, respectively) and quartz glass using a radiofrequency (RF) sputtering system (SRN-120, SORONA, South Korea). A heavily doped Si wafer was used for the Metal–Insulator–Semiconductor (MIS) capacitor device measurements, whereas quartz was used for the transmittance and energy bandgap measurements. The Si substrates had a resistivity below 0.005 Ω·cm and thicknesses between 500 and 550 μm. Before deposition, 15×15 mm^2 substrates were subjected to ultrasonic cleaning in isopropyl alcohol (IPA) for 10 min, rinsed with deionized (DI) water, and dried using nitrogen gas. A high-purity alumina target (99.95%, TASCO, USA) bonded to a copper backplate was used for the sputtering deposition, and the target-to-substrate distance was maintained at 15 cm. The process chamber of sputtering system was evacuated to a base pressure of 1×10^{-7} Torr using a dry pump for low vacuum and a cryogenic pump for high vacuum. Film deposition was performed at room temperature with a RF power of 600 W, a process pressure of 1.5×10^{-4} Torr, and an argon gas flow rate of 100 sccm. Alumina was deposited in two sequential layers of 100 nm each with a deposition time of 1650 s per layer, resulting in a total deposition time of 3300 s and a final film thickness of approximately 200 nm.

2.2. CF_4 plasma etching

The effect of CF_4 plasma etching on the Al_2O_3 films was evaluated using a high-density plasma system (SELEX 200, APTC, South Korea). This system integrates both capacitive and inductive coupling, enabling precise control of the ion energy and density of the reactive radicals. Plasma etching conditions were tailored to examine

the optical and dielectric properties, with different etching parameters selected to ensure clearer observations of the dielectric property changes. For optical studies, the upper RF power was held constant at 500 W, whereas the bottom RF power was varied from the as-deposited state to 150 W in increments of 50 W. The etching duration was set to 30 s with a CF_4 gas flow rate of 100 sccm and a process pressure of 15 mTorr. In contrast, for the dielectric studies, the upper RF power was fixed at 500 W, but the bottom RF power was increased to 150, 200, 250, and 300 W with an extended etching time of 60 s under the same gas flow and pressure conditions to induce more pronounced changes in the dielectric properties. After each plasma-etching cycle, the samples were allowed to cool for 10 min to ensure their thermal stability.

2.3. Characterization techniques

The etched films were systematically characterized to assess their physical, chemical, optical, and electrical properties. The crystallinity was analyzed using x-ray diffraction (XRD) with a New D8 Advance system (D8 DISCOVER, Bruker, USA). The chemical composition of the films was evaluated by XPS (NEXSA, Thermo-Fisher Scientific, USA), employing Al Kα radiation and calibration to the C 1 s peak at 284.8 eV. Curve fitting was performed with a Gaussian–Lorentzian peak shape following Shirley background subtraction. The optical properties, including the transmittance and energy bandgap changes, were investigated using a UV–vis spectrophotometer (Lambda 35, PerkinElmer, USA). Surface morphology and roughness were characterized using atomic force microscopy (AFM: NX-10, Park Systems, South Korea), and work function measurements were conducted using Kelvin probe force microscopy (KPFM). The electrical properties were examined using metal–insulator–semiconductor capacitors fabricated from 200 nm-thick Al_2O_3 films. Nickel top electrodes (5×5 mm^2) were deposited by DC sputtering (KVT-2004, KOREAVAC, South Korea) after plasma etching to analyze dielectric properties from the MIS capacitor. Electrical performance was evaluated using an Impedance analyzer (4294A, Agilent, Keysight, USA).

3. Results and discussion

To investigate the influence of RF bias power (applied to the bottom electrode) during the etching process on impurity incorporation and defect formation (oxygen or Al vacancies) in the remaining Al_2O_3 thin films, experiments were designed while keeping the other conditions fixed. Al_2O_3 films were etched using CF_4 plasma with an RF bias power ranging from 0 to 150 W in 50 W increments. XPS analysis was conducted to qualitatively assess the elemental composition and bonding states of the CF_4 plasma-etched Al_2O_3. Figure 1 shows the bonding ratios according to the binding energies of Al 2p in the sample before and after etching under RF bias power conditions ranging from 0 W to 150 W. The XPS profiles were calibrated using the C 1 s peak (284.8 eV) and adjusted considering the Al 2p peak. In figure 1, the Al 2p spectrum of the etched sample reveals three distinct peaks at approximately (74.2–74.6 eV), (75.2–75.8 eV), and (76.3–76.9 eV), corresponding to Al-O, F-Al-O, and Al-F bonds, respectively [21, 22]. Compared to the as-deposited sample, the CF_4 plasma-etched samples have the F-Al-O bonds and Al-F bonds because of the addition of F. With increasing bias power, the Al-F bonding concentration became more pronounced, whereas the Al-O bond concentration decreased, indicating enhanced fluorination of the surface. Additionally, the F-Al-O peak shifted to a higher binding energy compared to the Al-O bond as the bias power increased, reflecting changes in the electronic environment due to stronger interactions with fluorine atoms (F-terminated dangling bond Al). To further investigate the chemical changes in the oxygen environment, the O 1 s spectra of the films under varying plasma power conditions are presented in figure S01. As the RF bias power increases, an apparent increase in the higher binding energy peak at ~532.0–533.0 eV is observed, accompanied by a slight reduction in the lattice oxygen peak near 530.5 eV. This trend suggests that CF_4 plasma exposure leads to partial disruption of Al–O lattice bonds and the emergence of non-lattice oxygen species, such as hydroxyl groups, adsorbed moisture, or oxygen bonded in Al–OH-like configurations. These results support the Al 2p spectral analysis presented in figure 1, which demonstrates the emergence of Al–F and F–Al–O bonding states at the expense of Al–O coordination. Collectively, the XPS analyses reveal that increasing plasma power promotes fluorine incorporation into the Al_2O_3 film, accompanied by a systematic decrease in Al–O bonding and the formation of new Al–F and F–Al–O bonding states, alongside an increase in non-lattice oxygen species.

From the Al 2p XPS profiles in figure 1, we calculated the bonding of Al 2p to the core peak for the five samples through fitting calculations. The corresponding values according to the bias power are shown in table 1. The Al-O bonding ratio decreased from 100% to 48.8% as the bias power increased. In addition, the F-Al-O bonding ratio decreases from 40.1% to 35.7%, whereas the Al-F bonding ratio increases to 15.5%. As the bias power increased at 50 W intervals, the ratio of Al-F bonds to Al-O bonds gradually increased from 0% at first to 3.5%, 7.9%, and 20.2%, respectively, and finally, the maximum value was 31.8%, indicating that the Al-F bonding area concentration was higher than that of the Al-O bonding area under the condition of 150 W bias

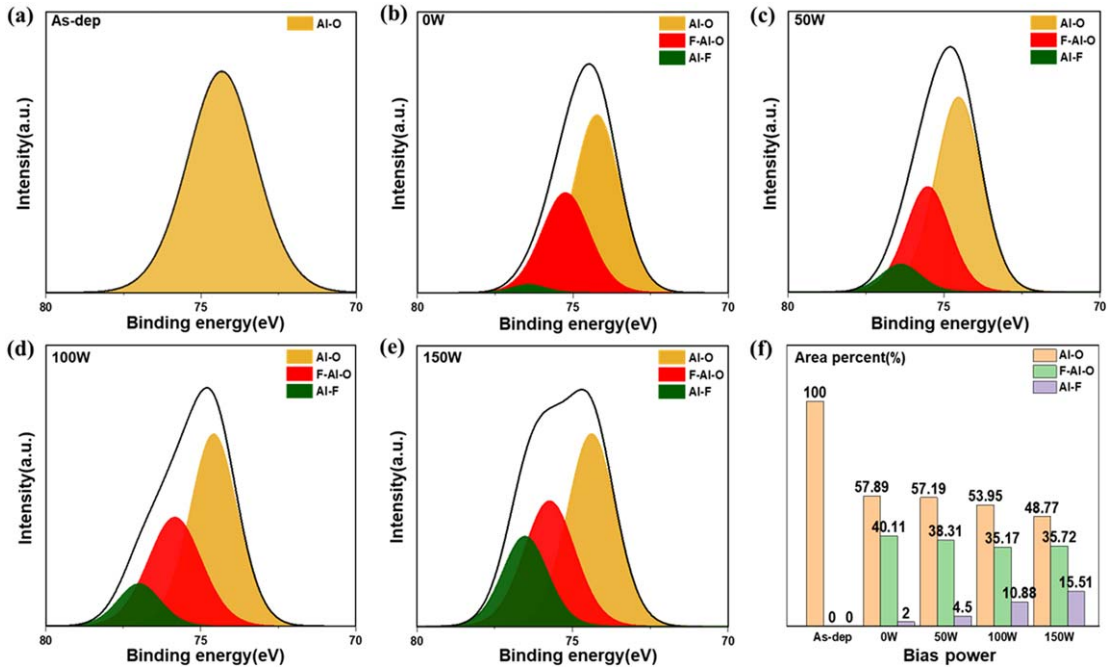

Figure 1. Fluorination effect on Al_2O_3 samples: (a)–(e) Al 2p XPS spectra of as-deposited and CF_4 plasma-etched samples (0–150 W), and (f) area percentage of Al–O, F–Al–O, and Al–F components.

Table 1. The bonding concentration from Al 2p XPS profiles (XPS analysis of as-deposited and CF_4 plasma-etched samples) and the ratio of Al–F bonding area to Al–O bonding area.

Bias power (W)	Al-O (%)	F-Al-O (%)	Al-F (%)	Al-F/Al-O ratio (%)
As-deposited	100.0	0	0	—
0	57. 9	40.1	2.0	3.5
50	57.2	38.3	4.5	7.9
100	54.0	35.2	10.9	20.2
150	48.8	35.7	15.5	31.8

power. As shown in figure S02, the XPS analysis revealed that the atomic percentage of Al 2p decreased with increasing bias power compared with the as-deposited sample. Al vacancies have a greater effect on charge density than O vacancies, requiring a greater formation energy [23, 24]. This suggests that under the same conditions, oxygen vacancies are more likely to form than aluminum vacancies. A higher charge density indicates a stronger attraction of electrons from the surrounding environment. When an aluminum vacancy forms, the site loses electrons, leading to a decrease in charge density and an increase in binding energy [25]. As shown in figure S02, the atomic percentage of Al decreased from 40.2% to a minimum of 37.8% as the bias power increased. Additionally, the shift of the Al 2p peak to a higher binding energy than that of the as-deposited sample suggests a potential correlation between the bias power and the increased formation of aluminum vacancies. The GIXRD results for the alumina thin films at various bias powers are shown in figure S03. The absence of noticeable peaks at any bias power indicated that the amorphous phase was maintained.

Figure 2(a) shows that the transmittance of the Al_2O_3 thin film, compared to the as-deposited state, shifts to longer wavelengths (red shift) for all bias powers. However, as the bias power increases, the peak intensity shifts to shorter wavelengths. This indicates widening of the bandgap. These results are due to the increase in Al vacancies and changes in the Al-F bonding concentration, respectively. As the bias power increased, the intensity of ion bombardment increased. This leads to the creation of Al vacancies due to the ion bombardment of the CF_4 plasma under various bias conditions. Figure 2(b) shows the optical bandgap calculated from the transmittance using the Tauc plot in equation (1):

$$(\alpha h\nu)^{1/n} = A(h\nu - E_g), \tag{1}$$

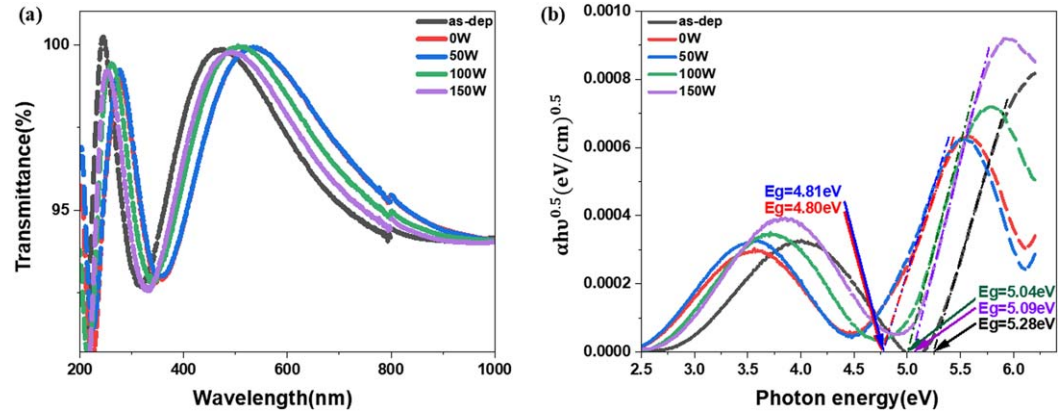

Figure 2. (a) The transmittance of the Al_2O_3 films and (b) optical bandgap of the Al_2O_3 films measured by UV–vis spectrophotometry.

where α is the absorption coefficient, h is Planck's constant, ν is photon's frequency, A is a parameter that depends on the transition probability, E_g is the bandgap, and n is the nature of the electronic transition [26–28]. The type of electronic transition (direct or indirect) determined n. We can use the value of n as 2, because there are many indirect transitions in amorphous Al_2O_3 films [26, 29]. Also, the curve $(\alpha h\nu)^{1/2}$ versus $h\nu$ calculated by transmittance has two peaks in Al_2O_3 films. The first transition, located at low energy, implies an optical gap where the formation of electron–hole pairs (EHPs) coupled with optical absorption (i.e., Frenkel excitons) begins [27]. The second transition corresponded to the fundamental energy gap; the results are shown in figure 2(b). We used the second transition to determine the energy bandgap by finding the x-axis intercept at $(\alpha h\nu)^{\frac{1}{2}} = 0$ on the linear extrapolation of the curve. The bandgap values obtained using Tauc's method are 5.28, 4.80, 4.81, 5.04, and 5.09 eV for the as-deposited, 0, 50, 100, and 150 W-etched samples, respectively. When the bias power increases, the bandgap energy clearly increases from 4.80 eV to 5.09 eV except for as-deposited sample. As shown in table 1, as the RF bias power increased from 0 W to 150 W, the area ratio of the Al-F bonds increased, while the area ratio of the Al-O bonds mostly decreased. This means that more fluorine was introduced into the Al_2O_3 film with increasing bias power. As a result, the aluminum-oxygen bonds were replaced by aluminum-fluorine bonds. This bond translation increases the bandgap. This is because the bandgap can be expanded for two reasons. First, fluorination arises from crystal field enhancement due to alterations in the nature of bonds. Second, valence charge transport occurs on the Al_2O_3 surface [30]. As a result, the Al-O bonds with smaller binding energy (512 ± 4 KJ mol^{-1}) were replaced by Al-F bonds (664 ± 6 KJ mol^{-1}) with larger binding, resulting in expanded bandgaps [30, 31]. In contrast, the as-deposited sample showed a larger bandgap (5.28 eV) than CF_4 the etched samples. This is because plasma etching results in a higher concentration of aluminum vacancies compared with the as-deposited thin film [32]. As fluorination progressed, etching of the Al_2O_3 film reduced the proportion of Al, which subsequently affected the bandgap variation. The increase in aluminum vacancies degraded the optical properties of the alumina thin films, demonstrating the effect of CF_4 plasma etching compared with the as-deposited sample. Except for the as-deposited sample, the bandgap expanded after CF_4 plasma etching, reducing the relative bonding ratio of aluminum to oxygen while enhancing the effect of fluorine. This indicates that the fluorination of the film slightly improved the optical properties of the alumina thin films. In other words, a higher bias power plays a role in alleviating the bandgap reduction caused by an increase in Al vacancies during the CF_4 etching process.

The work function of the alumina thin films was determined using Kelvin Probe Force Microscopy (KPFM), which was conducted using Atomic Force Microscopy (AFM) and a specialized EFM probe. This method evaluates the surface potential distribution by applying a sinusoidal voltage between the probe and material surface. The direct-current component was adjusted to counteract the potential difference and ensure accurate measurements of the surface characteristics. The work function was calculated as follows:

$$\phi_{\text{sample}} = \phi_{\text{Tip}} - V_{\text{CPD}} \tag{2}$$

In this expression, ϕ_{sample} denotes the work function of the material, ϕ_{Tip} corresponds to the probe's work function, and V_{CPD} is the contact potential difference measured by KPFM. Calibration was performed using standard gold and aluminum reference samples (PFKPFM-SMPL; Bruker, USA). The work function of the alumina thin films was measured under varying bias powers during the CF_4 plasma etching process. The results indicate that the work function systematically increased with increasing bias power. Specifically, the work function increased from 4.11 eV in the as-deposited state to 4.17 eV at 0 W, 4.18 eV at 50 W, 4.37 eV at 100 W, and 4.38 eV at 150 W after CF_4 plasma etching process. This increase in the work function is attributed to the passivation of oxygen vacancies by fluorine introduced during the CF_4 plasma etching process [33, 34]. Oxygen

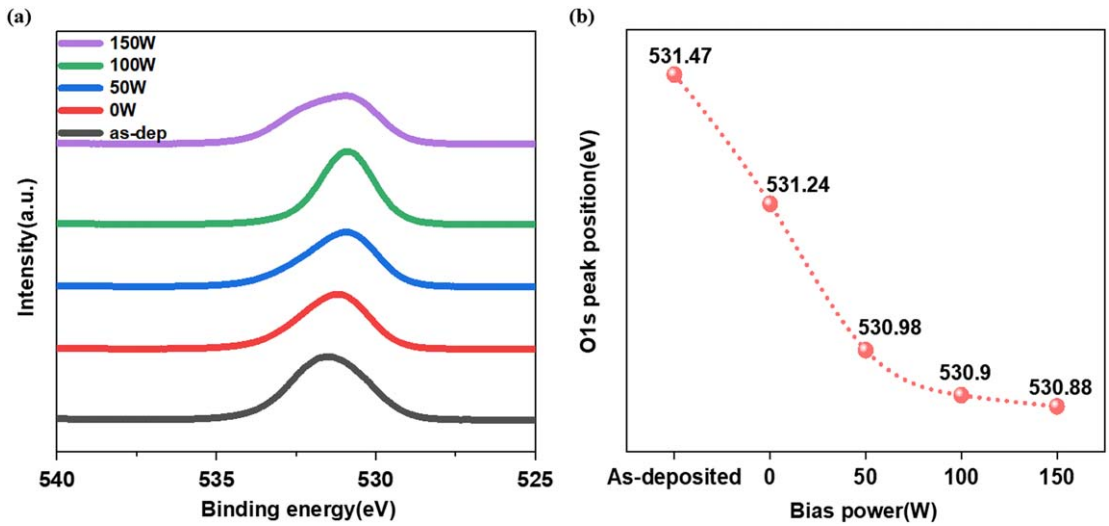

Figure 3. (a) Binding energy positions of O 1 s peak in as-deposited and CF_4 plasma-etched samples (0–150 W), and (b) plasma-induced shift in O 1 s peak position: trend and scatter plot analysis.

vacancy formation in metal oxides is typically associated with electron doping, which shifts the Fermi energy level upwards. However, fluorine passivation reduces the concentration of oxygen vacancies, which diminishes the associated electron-doping effect. This change results in a downward shift in the Fermi level and an increase in the work function of the material [33]. XPS can be used to study this phenomenon because the binding energy is indicative of the energy gap between the occupied electronic state and the Fermi level.

Figure 3(a) shows the XPS O 1 s spectra for each bias power, showing a gradual decrease in the binding energy of the O 1 s peak with increasing bias power, as shown in figure 3(b). The as-deposited sample exhibited the highest binding energy for the O 1 s peak, indicating that it had the most oxygen vacancies and represented the highest Fermi level. In contrast, during CF_4 plasma etching process, passivation of the oxygen vacancies occurs, leading to a decrease in the binding energy of the O 1 s peak. This reflects a reduction in the defect-related states and a simultaneous decrease in the Fermi level. Although XPS cannot directly detect missing oxygen atoms, changes in the binding energy provide indirect evidence of the reduction in oxygen vacancies. This behavior provides direct evidence that oxygen vacancies are effectively passivated under higher bias power conditions during the plasma etching process.

Valence band measurements (VBM) obtained by XPS reflect the energy difference between the Fermi level and the maximum valence band. Initially, the Fermi level to the maximum valence band energy for the as-deposited state was measured at 3.28 eV. This value increased significantly after CF_4 plasma etching, as shown in figure 4. Specifically, the E_F - E_{Vmax} rose from 3.28 in the as-deposited state to 3.55 eV after CF_4 plasma etching process at 0 W, 4.17 eV at 50 W, 4.41 eV at 100 W, and 4.64 eV at 150 W. Defects in Al_2O_3 create defect levels near the valence band and cause structural relaxation, altering atomic distances based on charge states [35]. Similarly, in Li-doped NiO, Li^+ doping weakens the Ni-O bonds, increasing the bond distance and positively shifting the valence band maximum [36]. Thus, defects and doping influenced the atomic structure, leading to valence band maximum shifts.

Figure 5 shows the band structure considering the energy bandgap, work function, and Fermi level to the valence band maximum. The numerical values corresponding to each aspect shown in figure 5 are listed in table 2. The distance from the minimum conduction band to vacuum level, calculated using the optical bandgap, Fermi level to valence band maximum and work function, increased from 2.11 eV in the as-deposited state to 2.92 eV at 0 W, 3.54 eV at 50 W, 3.74 eV at 100 W, and 3.93 eV at 150 W. As the bias power increased during the CF_4 plasma etching process, the electron affinity of the Al_2O_3 thin films increased owing to the substitution of Al-O bonds with Al-F bonds. This shift occurs because fluorine has a significantly higher electron affinity than oxygen.

Figure 6(a) illustrates the dielectric constant of the thin films etched with CF_4 plasma under various bias power conditions (150, 200, 250, and 300 W) compared with that of the as-deposited films (As-dep) plotted against frequency. The frequency range can be divided into two polarization mechanisms: space-charge (or interfacial) polarization ($<10^3$ Hz) and Dipole Polarization (10^3–10^7 Hz) [28]. Space Charge Polarization occurs owing to the accumulation of interfacial and defect charges, resulting in high capacitance in the low-frequency regions, which gradually decreases owing to slow charge movement. In contrast, Dipole Polarization occurs when molecules with dipole moments are aligned with an external electric field. In the intermediate frequency

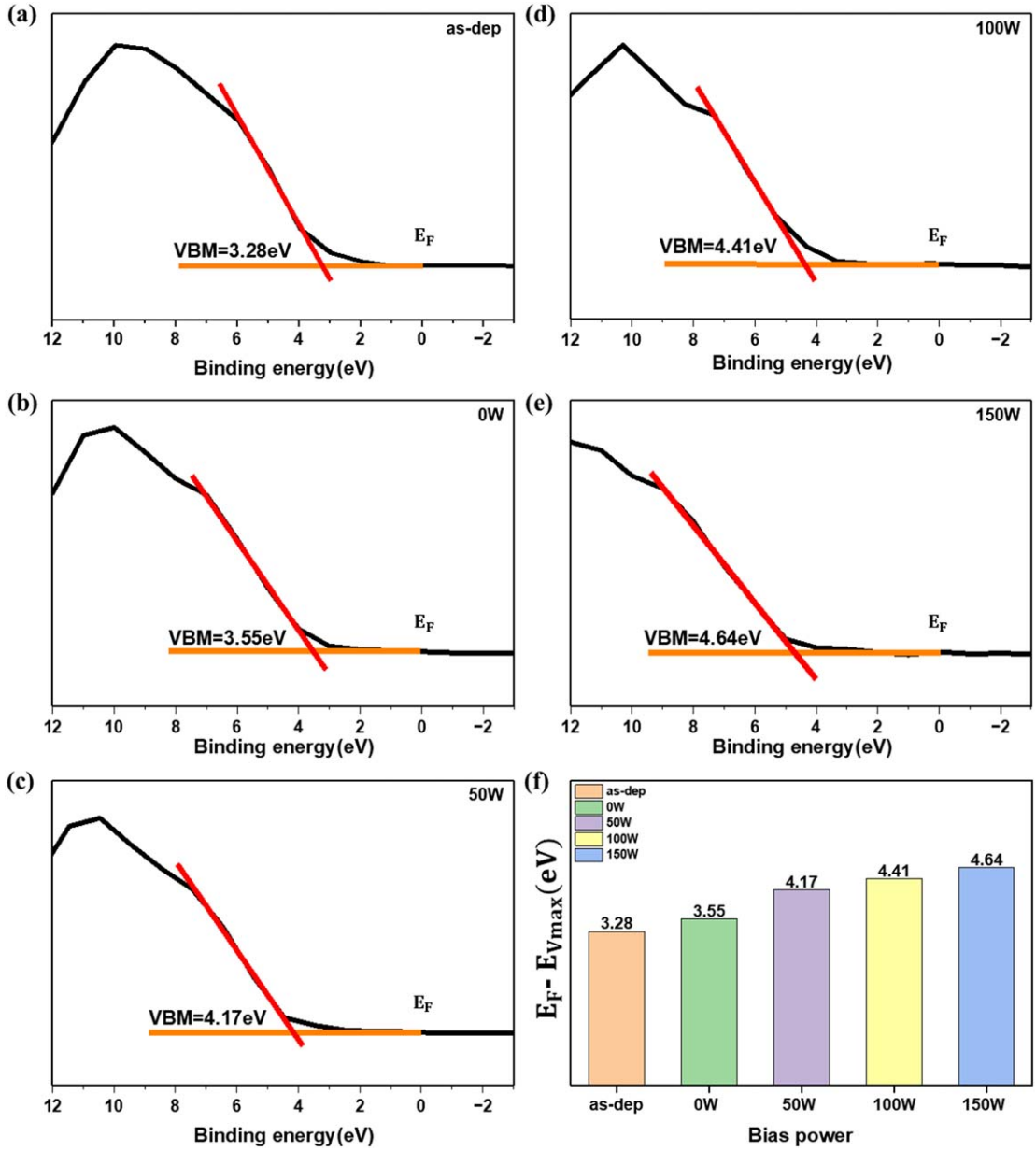

Figure 4. Valence band measurements by XPS: (a) as-deposited, (b) 0 W, (c) 50 W, (d) 100 W, (e) 150 W, and (f) bar chart of E_F–E_{Vmax}.

range, the capacitance remains constant; however, at higher frequencies, the rapidly changing electric field prevents the dipoles from aligning, leading to a decline in the capacitance. This behavior explains the observed trends. The Space Charge Polarization region below 1000 Hz represents the state before the dipoles align, where changes in the dielectric constant occur owing to external factors, such as interfacial charges and defect charges. Therefore, the region of focus was the Dipole Polarization (10^3–10^7 Hz). As shown in figure 6(a), within this range, the dielectric constant decreased with increasing bias power. This can be attributed to the greater incorporation of fluorine radicals from the CF_4 plasma into the thin film with increasing bias power. A previous study highlighted the significant effect of fluorine incorporation into Al_2O_3 thin films on their optical properties. An analysis based on the Sellmeier equation showed that as the fluorine doping concentration increased, the Al-O bonds were progressively replaced by Al-F bonds [37]. Based on these findings, this study provides a detailed analysis of the mechanism underlying the reduction in the dielectric constant of thin films. The resonance frequency (ω_0) is defined as shown in equation (3):

$$\omega_0 = \sqrt{\frac{k}{M}} \quad \text{and} \quad \frac{1}{M} = \frac{1}{M_+} + \frac{1}{M_-}, \tag{3}$$

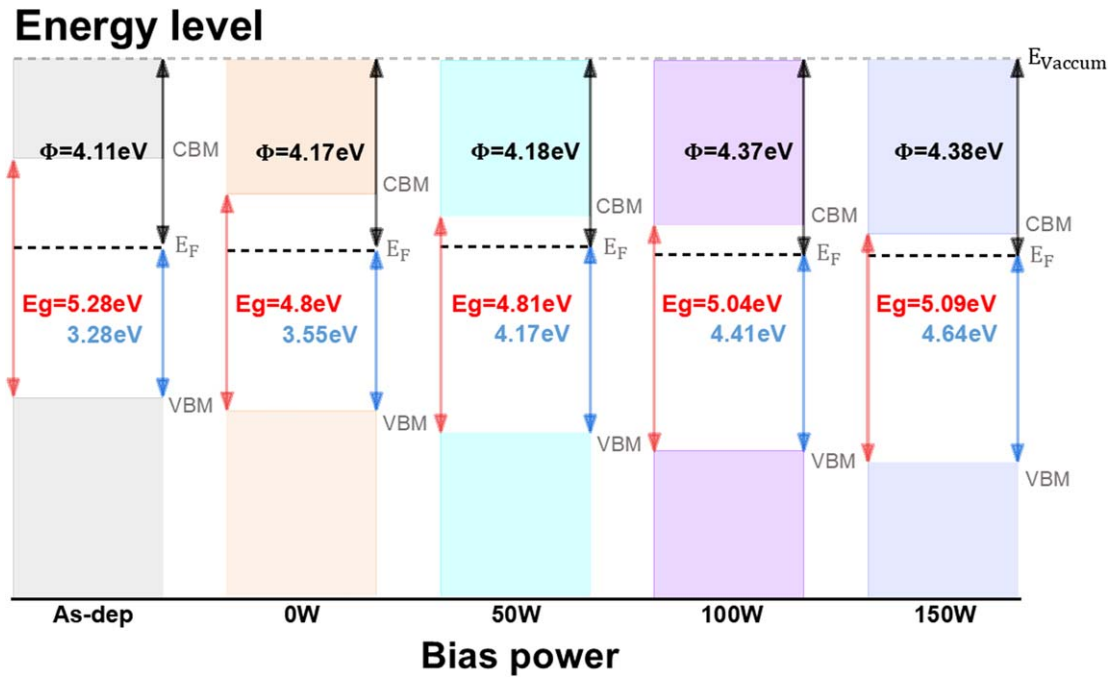

Figure 5. Band structure diagrams: As-deposited, 0 W, 50 W, 100 W, and 150 W.

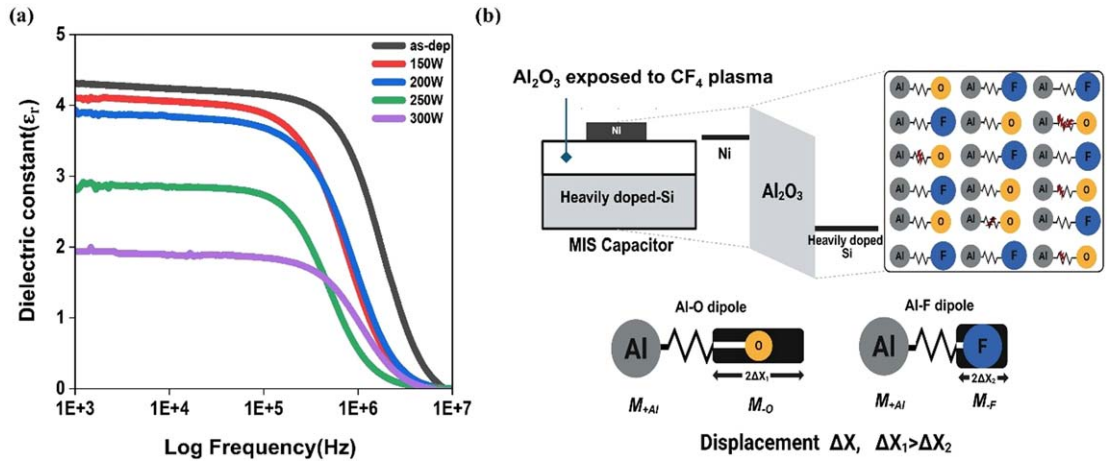

Figure 6. (a) Dielectric Constant–Log frequency plots according to bias powers. (b) Schematic model of F incorporated in Al_2O_3 films. Oxygen atoms of Al–O dipoles are replaced by the incorporation of F, forming Al–F dipoles, which causes a lowering of the dielectric constant.

Table 2. Optical bandgap, Work function (ϕ), E_F - E_{Vmax} and χ of the as-deposited, 0 W, 50 W, 100 W, and 150 W Al_2O_3 thin films.

Bias power (W)	Optical bandgap (eV)	Work function (eV)	E_F - E_{Vmax} (eV)	χ (eV)
As-deposited	5.28	4.11	3.28	2.11
0	4.80	4.17	3.55	2.92
50	4.81	4.18	4.17	3.54
100	5.04	4.37	4.41	3.74
150	5.09	4.38	4.64	3.93

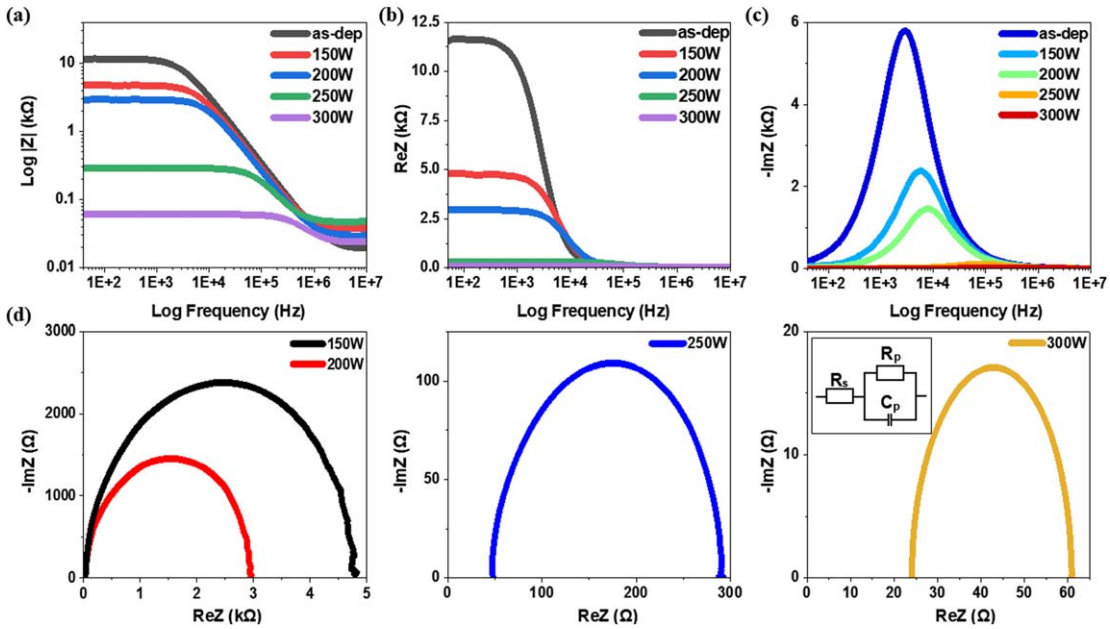

Figure 7. (a) Log|Z|–Log frequency, (b) Re(Z)–Log frequency, and (c) -Im(Z)–Log frequency plots at various bias powers. (d) Cole–Cole plots at various bias powers.

where k denotes the spring constant, and M, M_+, and M_- represent the ionic reduced mass, the mass of the positive ion, and the mass of the negative ion, respectively. Additionally, the displacement polarizability(α^{dis}) is expressed as shown in equation (4):

$$\alpha^{dis} = \frac{e}{M(\omega_0{}^2 - \omega^2)} \tag{4}$$

Figure 6(b) illustrates the dipole structures of the Al-O and Al-F bonds, which exhibit inherent resonance frequencies akin to a spring system, where M_{+Al}, M_{-O}, and M_{-F} represent the masses of the Al, oxygen, and fluorine atoms, respectively [22]. More fluorine was incorporated into the thin film as the RF bias power increased, resulting in the conversion of the Al-O bond to the Al-F bond, as discussed in the XPS results in figure 1. In this process, the larger mass of fluorine ions (M_-) compared to that of oxygen ions induces a greater dipole mass (M). According to equation (3), this leads to a lower resonance frequency (ω_0) of the dipole and a smaller displacement (ΔX). Consequently, as described in equation (4), the displacement polarizability (α^{dis}) of Al-F bonds becomes lower than that of Al-O bonds. As a result, with increasing bias power, the conversion of Al-O bonds to Al-F bonds results in a reduced dipole moment, which in turn decreases the relative dielectric constant of the thin film. Another factor contributing to the reduced dielectric constant is the formation of AlO_xF_y phases [21]. According to XPS results, before CF_4 plasma etching process, Al-O bonds are distributed throughout the dielectric region. However, after CF_4 plasma etching process, the appearance of F-Al-O area was observed to form when compared to the as-deposited sample. As the bias power increases, the area ratio of the Al-F bond increases. This suggests that increasing the bias power promotes the formation of an additional fluorine-combined layer within the dielectric region, rather than pure Al_2O_3. These phases contribute to lowering the dielectric constant of the thin film. This indicates that the formation of the AlO_xF_y layer weakens the overall dipole alignment of the dielectric. Therefore, CF_4 plasma etching process replaces part of the Al_2O_3 matrix with AlO_xF_y, which has a lower dielectric constant than pure Al_2O_3, further decreasing the overall dielectric constant.

To investigate the electrical properties of the CF_4 plasma-etched amorphous alumina thin films, impedance spectroscopy was employed in the frequency range 40–10 MHz. To confirm certain trends in the plasma etching process, the films were subjected to plasma bias powers varying from 150 to 300 W. As the bias power increased, the overall impedance of the system decreased, indicating enhanced electrical conductivity of the films under higher power conditions, as depicted in figure 7(a). To analyze the impedance characteristics, the real component (Z′) is plotted against the imaginary component (Z″) of the impedance, forming a Cole–Cole plot. This type of plot, which is characteristic of the Debye relaxation [38, 39], typically exhibits a semicircular shape, as shown in figure 7(d). The single semicircle observed for all measured conditions suggests the dominance of a single relaxation mechanism. The slight deviations from a perfect semicircle can be attributed to variations in the film density and defect distribution induced by the CF_4 plasma etching process. Assuming a single relaxation

Table 3. The R_S, R_P, C_P, F_{max} and τ values extracted from the fitting of the data for each bias power.

Bias power (W)	R_S (Ω)	R_P (kΩ)	C_P (nF)	F_{max} (kHz)	τ (μsec)
150	38.52	4.76	5.79	5.77	27.6
200	29.97	2.92	6.51	8.38	19.0
250	48.27	0.24	8.82	73.8	2.16
300	24.05	0.04	12.50	349	0.46

time, the MIS capacitor can be modeled as a circuit with a series contact resistance (R_S) and a parallel combination of bulk resistance (R_P) and bulk capacitance (C_P). This model effectively represents the electrical behavior of a system. The impedance of this model is given by

$$Z = \frac{1}{Y} = \frac{1}{G + i\omega C} = \frac{1}{\frac{1}{R} + i\omega C}, \tag{5}$$

where Y, G, and C represent admittance, conductance, and capacitance, respectively. The complex impedance (Z^*) of the equivalent circuit is represented as follows: [38, 40–43]

$$Z^* = R_s + \frac{R_p}{1 + i\omega R_p C_P} = Z' + iZ'' = ReZ + iImZ \tag{6}$$

$$ReZ = Z' = R_s + \frac{R_P}{1 + (\omega R_p C_P)^2} \tag{7}$$

$$ImZ = Z'' = \frac{\omega R_p^2 C_p}{1 + (\omega R_p C_P)^2} \tag{8}$$

The Cole–Cole plot, which displays the real component versus the imaginary component of the complex impedance, typically forms a semicircle when the system exhibits ideal Debye-type relaxation behavior. This semicircle reflects a specific dielectric relaxation process with a single relaxation time and can be described by the following expression:

$$\left[ReZ - \left(R_s + \frac{R_p}{2}\right)\right]^2 + (-ImZ)^2 = \left(\frac{R_p}{2}\right)^2 \tag{9}$$

This equation represents a circle centered at ($R_S + R_P/2$, 0) with a radius of $R_P/2$, corresponding to an ideal dielectric relaxation behavior. At higher frequencies, the lowest value of Z (real part of the impedance) reflected the series contact resistance (R_S). In contrast, at lower frequency ranges, the maximum value of Z', corresponds to the sum of the contact resistance (R_S) and the bulk resistance (R_P).

Table 3 provides an overview of the extracted R_S, R_P, C_P, F_{max}, and τ values obtained through fitting single arcs across bias powers ranging from 150 W to 300 W. As the bias power increased, a noticeable decrease in R_P was observed. This behavior can be attributed to the increased concentration of carriers introduced into the capacitor under increased power [39, 44–48]. Direct CF_4 plasma etching of the Al_2O_3 surface effectively reduced the interface trap state [21]. In figure 7(a), the crossover of the impedance values at higher frequencies indicates that the contact resistance (R_S) becomes dominant, as explained earlier. This behavior aligns with the modeled equation. Figures 7(b) and (c) illustrate the variations of Z' and Z'' with frequency under different power conditions. As shown in figure 7(b), Z' remains constant up to a specific frequency for each bias power, after which it decreases as the frequency increases. This behavior at low frequencies can be attributed to the dominance of space-charge polarization. At higher frequencies, Z' becomes independent of frequency. These results suggest that Z' exhibits a single relaxation process, as evident in the overall trend. The variation in the imaginary part of the impedance (Z'') with the frequency at different bias powers is shown in figure 7(c). As shown in figure 7(c), the Z'' values for each bias power initially increased with frequency, reaching a maximum before decreasing. This frequency-dependent behavior of Z'' reflects the presence of a single relaxation process in the device. The peak position of Z'' shifted towards higher frequencies as the applied bias power increased. This shift was associated with a decrease in the bulk resistance of the device as the bias power increased. Accordingly, the relaxation time ($\tau = 1/2\pi f_{max} = 1/\omega_{max}$) of the MIS capacitor was calculated from the frequency corresponding to the maximum peak. Table 3 provides the relaxation time (τ) and F_{max} values for each bias power. The relaxation time τ shows a decreasing trend with increasing bias power, which is attributed to the enhanced injection of charge carriers into the capacitor.

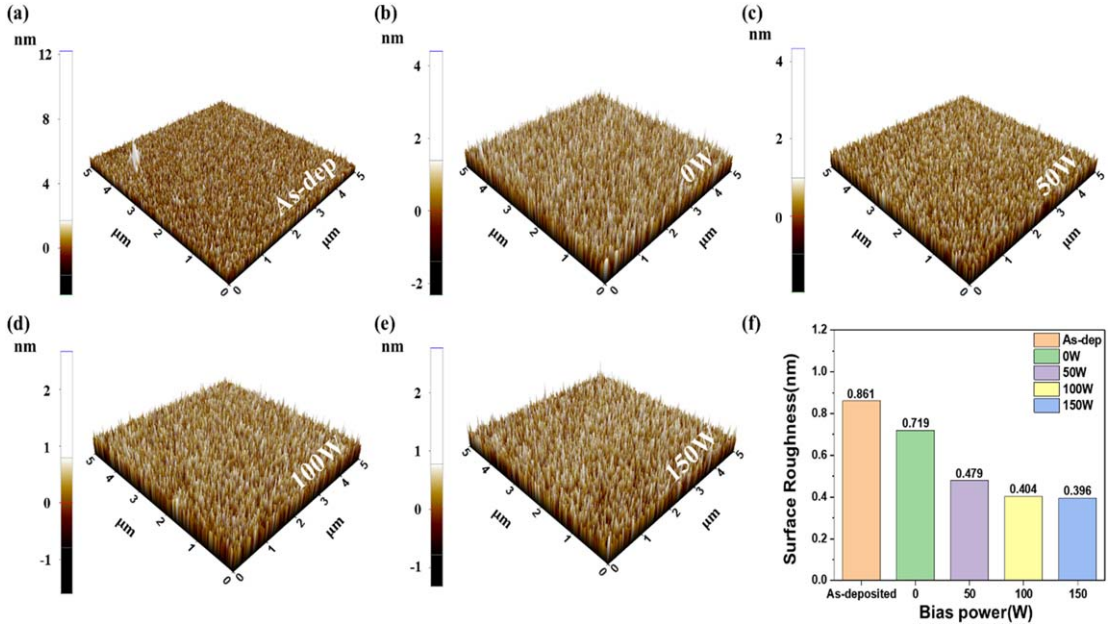

Figure 8. AFM images showing variations in the Al_2O_3 films with RF bias power: (a) as-deposited, (b) 0 W, (c) 50 W, (d) 100 W, and (e) 150 W. (f) Bar chart of surface roughness.

To investigate the effect of CF_4 plasma etching on the surface roughness of the Al_2O_3 films, experiments were conducted under the following conditions: The samples were etched with CF_4 plasma for 30 s at various bias powers (0, 50, 100, and 150 W). In this experiment, an as-deposited Al_2O_3 film served as the reference sample. The root mean square (RMS) surface roughness was measured using atomic force microscopy (AFM) before and after plasma etching. The AFM results of this experiment are shown in figure 8. The RMS roughness decreases from 0.861 nm (as-deposited) to 0.719 nm at 0 W, 0.479 nm at 50 W, 0.404 nm at 100 W, and 0.396 nm at 150 W. This indicates that the RMS surface roughness significantly decreased in the CF_4 plasma-etched samples compared with that in the as-deposited samples, and the roughness value gradually decreased as the bias power increased [49]. Additionally, another experiment was conducted in which the samples were etched for 60 s at higher bias powers (150, 200, 250, and 300 W). The AFM results of this experiment are shown in figure S04. In this experiment, a consistent reduction in RMS surface roughness was observed. These results demonstrate that the CF_4 plasma etching process can effectively reduce the surface roughness of Al_2O_3 films. The enhancement of ion energy with increasing bias power plays a crucial role in promoting ion-assisted surface reactions, leading to an improved surface morphology.

4. Conclusion

In this study, we systematically investigated the effects of CF_4 plasma etching on the structural, optical, and electrical properties of Al_2O_3 thin films, focusing on the impact of the defect dynamics of the thin films during the etching process on the material properties. The experimental results demonstrated that plasma etching induced specific defect structures that substantially altered the chemical bonding configuration, optical band structure, and electrical properties of the Al_2O_3 films. XPS analysis revealed progressive substitution of Al-O bonds with Al-F bonds during plasma etching. This substitution mechanism reduced the oxygen vacancy concentration while establishing fluorine-rich bonding environments. The transformation of the chemical bonding structure induced modifications in the electronic band structure, resulting in an increase in the work function with increasing RF bias power and changes in the optical bandgap. Electrical characterization via dielectric measurements demonstrated a systematic reduction in the dielectric constant with increasing RF bias power. This phenomenon could be attributed to the changes in the dipole moments due to conversion from Al-O to Al-F. Furthermore, the carrier concentration increased, while the interface trap density decreased. This comprehensive investigation established a distinct correlation between the defect dynamics due to CF_4 plasma etching and the resultant modifications in the Al_2O_3 thin-film properties. These results provide valuable insights for optimizing plasma processing parameters and controlling plasma-induced modifications, and are expected to open avenues for developing advanced electronic and optoelectronic devices.

CRediT authorship contribution statement

Yu-Bin An: Conceptualization, Validation, Investigation, Data Curation, Visualization, Writing - original draft. **Da-Won Ryu:** Conceptualization, Methodology, Investigation. **Seung-Hyun Ma:** Conceptualization, Methodology, Investigation. **Dong-Geon Lee:** Methodology, Investigation. **Mi-Jin Jin:** Investigation, Resources, Writing - Review & Editing. **Doo-Seung Um:** Conceptualization, Methodology, Resources, Visualization, Writing - Review & Editing, Supervision. **Chang-Il Kim:** Conceptualization, Writing - Review & Editing, Supervision, Project administration, Funding acquisition.

Acknowledgments

This work was supported by Korea Institute for Advancement of Technology (KIAT) grant funded by the Korea Government (MOTIE) (P0023718, Inorganic Light-emitting Display Expert Training Program for Display Technology Transition), and by the Institute for Basic Science (IBS-R019-Y1).

Conflict of interest

The authors declare that they have no conflict of interests.

Data availability statement

All data that support the findings of this study are included within the article (and any supplementary files).

Appendix. Supplementary material

Supplementary data to this article can be found online at https://

ORCID iDs

Yu-Bin An https://orcid.org/0009-0002-2100-3318
Mi-Jin Jin https://orcid.org/0000-0001-7570-262X
Doo-Seung Um https://orcid.org/0000-0003-4085-4580

References

[1] Arts K, Hamaguchi S, Ito T, Karahashi K, Knoops H C M, Mackus A J M and Kessels W M M 2022 Foundations of atomic-level plasma processing in nanoelectronics *Plasma Sources Sci. Technol.* **31** 103002
[2] Oehrlein G S *et al* 2024 Future of plasma etching for microelectronics: challenges and opportunities *J. Vac. Sci. Technol. B* **42** 041501
[3] Eriguchi K 2017 Modeling of defect generation during plasma etching and its impact on electronic device performance-plasma-induced damage *J. Phys. D: Appl. Phys.* **50** 333001
[4] Eriguchi K, Takao Y and Ono K 2011 Modeling of plasma-induced damage and its impacts on parameter variations in advanced electronic devices *J. Vac. Sci. Technol. A* **29** 041303
[5] Sato Y, Shibata S, Nishimura K, Yamasaki M, Murakami M, Urabe K and Eriguchi K 2022 Predicting the effects of plasma-induced damage on p–n junction leakage and its application in the characterization of defect distribution. *J. Vac. Sci. Technol. B* **40** 062209
[6] Mu X C, Fonash S J, Rohatgi A and Rieger J 1986 Comparison of the damage and contamination produced by CF_4 and CF_4/H_2 reactive ion etching: the role of hydrogen. *Appl. Phys. Lett.* **48** 1147–9
[7] Karzhavin Y and Wu W 1998 Plasma induced charging and physical damage after dry etch processing *3rd Int. Symp. on Plasma Process-Induced Damage (Cat. No. 98EX100)*
[8] Eriguchi K, Matsuda A, Takao Y and Ono K 2014 Effects of straggling of incident ions on plasma-induced damage creation in 'fin'-type field-effect transistors *Jpn. J. Appl. Phys.* **53** 03DE02
[9] Hashimoto K, Hikosaka Y, Hasegawa A and Nakamura M 1996 Reduction of the charging damage from electron shading *Proceedings of 1st International Symposium on Plasma Process-Induced Damage* (IEEE)
[10] Cheung K P and Chang C P 1994 Plasma-charging damage: a physical model. *J. Appl. Phys.* **75** 4415–26
[11] Eriguchi K and Ono K 2015 Impacts of plasma process-induced damage on MOSFET parameter variability and reliability *Microelectron. Reliab.* **55** 1464–70
[12] Wu I-W, Bruce R H, Koyanagi M and Huang T Y 1989 Degradation of gate oxide breakdown characteristics by electrostatic and radiation damage during plasma processing *International Symposium on VLSI Technology, Systems and Applications* (IEEE)
[13] Mizutani T 1996 Fundamental aspects of plasma-induced radiation damage Of SiO/sub 2//Si-A Review *Proceedings of 1st International Symposium on Plasma Process-Induced Damage* (IEEE)
[15] Weber J R, Janotti A and Walle C G V d 2011 Native defects in Al_2O_3 and their impact on III-V/Al_2O_3 metal-oxide-semiconductor-based devices *J. Appl. Phys.* **109**

[14] Ma T 2002 Plasma process induced radiation effects in CMOS technology *7th International Symposium on Plasma-and Process-Induced Damage* (IEEE)
[16] Robertson J and Wallace R M 2015 High-K materials and metal gates for CMOS applications *Materials Science and Engineering: R: Reports* **88** 1–41
[17] Yang X, Kim D-P, Um D-S, Kim G-H and Kim C-I 2009 Temperature dependence on dry etchinig of Al_2O_3 thin films in $BCl_3/Cl_2/Ar$ plasma *J. Vac. Sci. Technol. A* **27** 821–5
[18] Seidl H *et al* 2002 A fully integrated Al_2O_3 trench capacitor DRAM for sub-100 nm technology *Digest. International Electron Devices Meeting* (IEEE)
[19] Eklund P, Sridharan M, Singh G and Bottiger J 2009 Thermal Stability and Phase Transformations of γ-/Amorphous-Al_2O_3 Thin Films *Plasma Processes Polym.* **6** S907–11
[20] Larcher L, Padovani A, Puglisi F M and Pavan P 2018 Extracting atomic defect properties from leakage current temperature dependence *IEEE Trans. Electron Devices* **65** 5475–80
[21] Oh S, Kwon O, Kim M J, Seo W, Cho E, Park H K, Park W and Cho B 2025 Improving bias stability of IGZO field-effect transistors through CF_4 plasma treatment of Al_2O_3 dielectrics *Mater. Sci. Semicond. Process.* **185** 108927
[22] Fan K M, Lai C S, Peng H K, Lin S J and Lee C Y 2007 Improvements on interface reliability and capacitance dispersion of fluorinated ALD-Al_2O_3 gate dielectrics by CF_4 plasma treatment *J. Electrochem. Soc.* **155** G51
[23] Zeng J, Wu G, Shi W and Chen S 2019 First-principles study on properties of the native defects in Al_2O_3(110) surface *Protection of Metals and Physical Chemistry of Surfaces* **55** 631–6
[24] Zhang C-H, Chen B, Jin Y and Sun D-B 2018 A DFT study on the failure mechanism of Al_2O_3 film by various point defects in solution *Chem. Phys.* **504** 48–56
[25] Greczynski G and Hultman L 2020 X-ray photoelectron spectroscopy: towards reliable binding energy referencing *Prog. Mater Sci.* **107** 100591
[26] Barajas-Ledesma E, Garcia-Benjume M L, Espitia-Cabrera I, Ortiz-Gutierrez M, Espinoza-Beltran F J, Mostaghimi J and Contreras-Garcia M E 2010 Determination of the band gap of TiO_2–Al_2O_3 films as a function of processing parameters *Materials Science and Engineering: B* **174** 71–3
[27] Dongol M, El-Nahass M M, El-Denglawey A, Elhady A F and Abuelwafa A A 2012 Optical Properties of Nano 5,10,15,20-Tetraphenyl-21H,23H-Prophyrin Nickel (II) Thin Films *Curr. Appl Phys.* **12** 1178–84
[28] Kim J-Y, Jin M-J, Hou B, Kim M P, Um D-S and Kim C-I 2023 Reducing the oxygen vacancy concentration in $SrTiO_{3-\delta}$ thin films via an optimized O_2 plasma treatment for enhancing device properties *Appl. Surf. Sci.* **639** 158271
[29] Shi S, Qian S, Hou X, Mu J, He J and Chou X 2018 Structural and optical properties of amorphous Al_2O_3 thin film deposited by atomic layer deposition *Adv. Condens. Matter Phys.* **2018** 1–10
[30] Pan L K, Ee Y K, Sun C Q, Yu G Q, Zhang Q Y and Tay B K 2004 Band-gap expansion, core-level shift, and dielectric suppression of porous silicon passivated by plasma fluorination *J. Vac. Sci. Technol. B* **22** 583–7
[31] Li G, Zhao C, Yu Q, Yang F and Chen J 2024 Revealing Al–O/Al–F reaction dynamic effects on the combustion of aluminum nanoparticles in oxygen/fluorine containing environments: A reactive molecular dynamics study meshing together experimental validation *Defence Technology* **34** 313–27
[32] Rechtin M D 1979 A transmission electron microscopy study of the defect microstructure of Al_2O_3, subjected to ion bombardment *Radiat. Eff.* **42** 129–44
[33] Wang J, Mueller D N and Crumlin E J 2024 Recommended strategies for quantifying oxygen vacancies with x-ray photoelectron spectroscopy *J. Eur. Ceram. Soc.* **44** 116709
[34] Choi M and Walle C G V d 2023 Fluorine and related complexes in α-Al_2O_3 *J. Appl. Phys.* **134** 064501
[35] Asaduzzaman A 2022 Atomic-scale etching mechanism of aluminum with fluorine-based plasma *The Journal of Physical Chemistry C* **126** 14180–6
[36] Wei L, Jiang L, Yuan S, Ren X, Zhao Y, Wang Z, Zhang M, Shi L and Li D 2016 Valence band edge shifts and charge-transfer dynamics in Li-doped NiO based p-type DSSCs *Electrochim. Acta* **188** 309–16
[37] Lai C S, Fan K M, Peng S K, Lin S J, Lee C Y and Ai C F 2007 Fluorine effects on the dipole structures of the Al_2O_3 thin films and characterization by spectroscopic ellipsometry *Appl. Phys. Lett.* **90** 172904
[38] Maity S, Bhattacharya D and Ray S K 2011 Structural and impedance spectroscopy of pseudo-co-ablated $(SrBi_2Ta_2O_9)_{(1-x)}$–$(La_{0.67}Sr_{0.33}MnO_3)_x$ composites *J. Phys. D* **44** 095403
[39] Büyükbaş-Uluşan A and Tataroglu A 2020 Impedance spectroscopy of Au/TiO_2/n-Si metal-insulator-semiconductor (MIS) capacitor *Physica B* **580**
[40] Jeon S and Park S 2011 Analysis of interface trap density of metal–oxide-semiconductor devices with Pr_2O_3 gate dielectric using conductance method *Microelectron. Eng.* **88** 872–6
[41] Brus V V 2012 On the impedance spectroscopy of structures with a potential barrier *Semiconductors* **46** 1012–5
[42] Buyukbas-Uluşan A, Yeriskin S A, Tataroglu A, Balbasi M and Kalandaragh Y A 2018 Electrical and impedance properties of MPS structure based on (Cu_2O–CuO–PVA) interfacial layer *J. Mater. Sci., Mater. Electron.* **29** 8234–43
[43] Liu Y, Liu A, Hu Z, Liu W and Qiao F 2012 Impedance spectroscopy studies on CuPc/n-Si hybrid solar cell *J. Phys. Chem. Solids* **73** 626–9
[44] Trad H, Rouis A, Davenas J and Majdoub M 2014 Optical and electrical properties of bi-layers organic devices *Eur. Phys. J. Appl. Phys.* **68** 10103
[45] Bouzitoun M, Dridi C, Chaahane R B, Ouada H B, Gam H and Majdoub M 2016 Electrical properties of ITO/benzylated cyclodextrins (β-CDs (Bz))/Al diode structures *Sci. Technol. Adv. Mater.* **7** 772–9
[46] Braik M, Dridi C, Ali M B, Abbas M N and Errachid A 2015 Investigation of structural, optical and electrical properties of a new cobalt phthalocyanine thin films with potential applications in perchlorate sensor *Synth. Met.* **209** 135–42
[47] Chauhan G, Srivastava R, Tyagi P, Kumar A, Srivastava P C and Kamalasanan M N 2010 Frequency dependent electrical transport properties of 4,4′,4″-tris(N-3-methylphenyl-N-phenylamine)triphenylamine by impedance spectroscopy *Synth. Met.* **160** 1422–6
[48] Suman C K, Yun J, Kim S, Lee S-D and Lee C 2009 AC impedance spectroscopic studies of transport properties in metal oxide doped α-NPD *Curr. Appl Phys.* **9** 978–84
[49] Chen C-W, Cho W-H, Chang C-Y, Su C-Y, Chu N-N, Kei C-C and Li B-R 2022 CF_4 plasma-based atomic layer etching of Al_2O_3 and surface smoothing effect *Journal of Vacuum Science & Technology A* **41** 012602